

# Evolution of small-mass-ratio binaries with a spinning secondary

Niels Warburton,<sup>1</sup> Thomas Osburn,<sup>2</sup> and Charles R. Evans<sup>3</sup>

<sup>1</sup>*School of Mathematics and Statistics and UCD Institute for Discovery,  
University College Dublin, Belfield, Dublin 4, Ireland*

<sup>2</sup>*Department of Physics and Astronomy, Oxford College of Emory University, Oxford, Georgia 30054, USA*

<sup>3</sup>*Department of Physics and Astronomy, University of North Carolina, Chapel Hill, North Carolina 27599, USA*

We calculate the evolution and gravitational-wave emission of a spinning compact object inspiraling into a substantially more massive (non-rotating) black hole. We extend our previous model for a non-spinning binary [Phys. Rev. D 93, 064024] to include the Mathisson-Papapetrou-Dixon spin-curvature force. For spin-aligned binaries we calculate the dephasing of the inspiral and associated waveforms relative to models that do not include spin-curvature effects. We find this dephasing can be either positive or negative depending on the initial separation of the binary. For binaries in which the spin and orbital angular momentum are not parallel, the orbital plane precesses and we use a more general osculating element prescription to compute inspirals.

PACS numbers: 04.25.dg, 04.30.-w, 04.25.Nx, 04.30.Db

## I. INTRODUCTION

The era of gravitational wave astronomy has recently dawned [1–3], being ushered in by tremendous advances in experimental physics, data analysis, and theoretical source modeling. Source modeling is necessary, at minimum, for estimating the physical parameters of relativistic compact binary inspirals. It can also be required to even detect systems with comparable masses [2] and it is expected to be crucial for detection of extreme-mass-ratio binaries. For both detection and parameter estimation, searches are run over a large parameter space (using e.g., Monte-Carlo-based methods), at each step convolving the data with theoretical waveform templates. The signal-to-noise ratio (SNR) will only coherently grow with the number of oscillations in the signal if the phase of the template and the signal are closely matched, typically to less than one radian over the observed time span. Waveform templates that do not meet this requirement will result in a substantial loss of accuracy for parameter estimation, or even worse provide no detection at all. Tracking the signal phase to within one radian is a particularly stringent requirement for small mass-ratio systems which accumulate hundreds to many hundreds of thousands of radians of phase whilst in the detector band.

The gravitational waves emitted from the inspiral of a stellar mass black hole or other comparable mass compact object into a massive black hole with mass  $M \sim 10^4$ – $10^7 M_\odot$  are in the frequency band of the Laser Interferometer Space Antenna, LISA, which has recently been selected as the European Space Agency’s L3 mission [4]. These extreme mass-ratio inspirals (EMRIs) are key sources for LISA [5]. The information carried in the waveforms from EMRIs will allow us to precisely measure properties of massive black holes and their stellar environment as well as providing unprecedented tests of general relativity in the strong-field regime [6–10].

Another class of interesting systems involve intermediate mass black holes (IMBHs) with  $M \sim 10^2$ – $10^3 M_\odot$ .

Such black holes can form intermediate mass-ratio inspirals (IMRIs) that fall into two categories depending on whether there is a stellar mass compact object inspiraling into the IMBH or the IMBH is inspiraling into a massive black hole. The former will merge in the band of ground-based detectors if the chirp mass of the binary is  $\lesssim 350 M_\odot$  [11] (this is slightly increased for ground-based observatories beyond the advanced detector era [12, 13]). The inspiral phase of such binaries should also be detectable in LISA many weeks before their merger in the LIGO band [14, 15]. The second type of IMRI would be a very loud source in the LISA band (possibly not even requiring matched filtering to find [16]). As the population of IMBHs is poorly understood the event rates for both types of IMRIs are not well constrained [17]. For this reason we will concentrate our discussion around EMRIs whilst bearing in mind that IMRIs are an exciting potential class of sources that can be modeled with a similar setup.

The leading-order (in the mass-ratio) dissipative dynamics of EMRIs is now understood when the primary is rotating [18, 19] but has yet to be compiled into complete inspiral models (many so-called ‘kludge’ models have been developed [20] which use some of this information but to date the development of these models has been driven by the need to rapidly compute waveform templates to train data analysis algorithms rather than a need for high precision). Producing waveform models that track the phase evolution of the binary whilst it is emitting gravitational waves in LISA’s band to within one radian requires including subleading-order corrections to the orbital dynamics.

These subleading-order corrections include the following effects: (1) orbital resonances, (2) first-order conservative terms, (3) oscillatory first-order dissipative terms, (4) second-order in the mass-ratio, orbit-averaged dissipative contribution, and (5) spin-orbit coupling effects [21]. There has been great progress calculating some of these effects within black hole perturbation theory and, in particular, within the self-force program [22].

For geodesic equatorial motion we have calculations at first order in the mass ratio of conservative dynamics about non-rotating [23–30] and rotating black holes [31–35]. These results have been successfully compared and synergized with results from other approaches to the two-body problem [29, 31–33, 36–43]. Orbital resonances are known to be important [44–46] but a precise understanding of them awaits calculations for generic orbits about rotating black holes. Steady progress is also being made on second order in the mass-ratio calculations [47–56]. Including these various results into self-force inspiral models has also been an active field of research [57–59].

The primary focus of this work is to incorporate effects associated with the spin of the secondary into inspiral models for small mass-ratio systems. This has been explored previously using models incorporating post-Newtonian results [60, 61] and in models using strong-field self-force results restricted to quasi-circular inspirals [62]. In this work we compute the effect of spin-curvature coupling on generic inspirals into a non-rotating black hole.

The next section details the different drivers of an inspiral and highlights which ones we are including in our current model. The rest of the paper is organized as follows. In Sec. III we give an overview of our approach to modeling inspirals. In Sec. IV we describe the osculating element prescription we use, extending previous formulations to generic motion (not confined to the equatorial plane). In Sec. V we describe the calculation of the self-force and spin-curvature forcing terms. In Sec. VI we describe how, once we have the inspiral trajectory, we compute the associated waveform by moving through a sequence of so-called snapshot waveforms. In Sec. VII we give results for spin-aligned binaries where we observe the difference in the accumulated inspiral phase with respect to a non-spinning binary can be either positive or negative depending on the initial separation of the binary. In VIII we give results for spin-unaligned binaries which precess out of the equatorial plane. Finally, we give some concluding remarks in Sec. IX.

Throughout this work we will use geometrized units such that the speed of light and the gravitational constant are equal to unity ( $c = G = 1$ ). We will denote the mass of the primary by  $M$  and the mass of the secondary by  $\mu$ , and will adopt standard Schwarzschild coordinates  $x^\alpha = (t, r, \theta, \varphi)$ .

## II. PHYSICAL DRIVERS OF AN INSPIRAL

The physical mechanism of an inspiral can be viewed as a force that drives the secondary’s orbit away from geodesic motion in the (background) spacetime of the primary. This force has a non-local contribution arising from the body’s interaction with its own metric perturbation, commonly called the self-force. If the secondary is spinning there is an additional non-local contribution resulting from perturbing the orbit and the stress-energy

tensor of the body as well as a local contribution arising from the coupling between the spin of the body and the tidal field (background curvature) of the primary. The latter of these is the well-known Mathisson-Papapetrou-Dixon (MPD) spin-curvature force [63, 64]. By expanding the Einstein field equations perturbatively in powers of the mass ratio,  $\epsilon = \mu/M \ll 1$ , the equations of motion for the inspiraling body can be written as

$$\begin{aligned} \mu u^\beta \nabla_\beta u^\alpha = & \mu^2 \left( F_{\text{mono}}^{(1)\alpha} + \mu F_{\text{mono}}^{(2)\alpha} \right) \\ & + S \left( F_{\text{spin-curvature}}^\alpha + \mu F_{\text{dipole}}^{(1)\alpha} \right) \equiv F^\alpha, \end{aligned} \quad (2.1)$$

where  $u^\alpha$  is the body’s four-velocity,  $\nabla$  denotes the covariant derivative with respect to the background metric of the primary,  $S$  is the spin magnitude, and  $F^\alpha$  is the net force. By  $F^{(n)\alpha}$  we denote the  $n$ th-order self-force, i.e., the part proportional to the  $n + 1$  power of the mass ratio. The ‘mono/dipole’ subscripts denote whether the force arises from the mass or spin of the secondary respectively. The subscript ‘spin-curvature’ denotes the MPD force. As we discuss below, in Eq. (2.1) we have truncated the expansion in the mass ratio at high enough order to include all important effects.

When the secondary moves along a geodesic of the background spacetime the influence on the inspiral of the forces on the righthand side of Eq. (2.1) can be split into conservative (time-symmetric) and dissipative (time-antisymmetric) pieces such that

$$F^\alpha = F_{\text{diss}}^\alpha + F_{\text{cons}}^\alpha. \quad (2.2)$$

Conservative forces act to perturb the orbital parameters, but do not cause a secular decay of the orbit. The self-force has a conservative component and the leading-order MPD force  $F_{\text{spin-curvature}}^\alpha$  is also conservative in nature. Dissipative forces are responsible for radiation reaction effects that lead to, e.g., the decay of orbital energy and angular momentum. This secular decay can be calculated by averaging  $F_{\text{diss}}^\alpha$ , which motivates a decomposition of the net force into an adiabatic part,  $F_{\text{ad}}^\alpha$ , and an oscillatory part,  $F_{\text{osc}}^\alpha$

$$F^\alpha = F_{\text{ad}}^\alpha + F_{\text{osc}}^\alpha, \quad (2.3)$$

$$F_{\text{ad}}^\alpha \equiv \langle F_{\text{diss}}^\alpha \rangle, \quad (2.3)$$

$$F_{\text{osc}}^\alpha \equiv F^\alpha - \langle F_{\text{diss}}^\alpha \rangle. \quad (2.4)$$

The adiabatic part varies slowly over an inspiral on the radiation reaction timescale and represents some average over the orbital timescale (see [58] for details about an appropriate averaging procedure). The oscillatory part varies more rapidly on the orbital time scale.

A number of authors have considered how these different forces influence the phase of an inspiral [65–67] with one of the most rigorous discussions given by Hinderer and Flanagan [21]. We now briefly review several key results and highlight where previous work has employed the various components of the self-force in computing inspirals.

EMRIs accumulate tens to hundreds of thousands of radians of orbital phase whilst the binary is in the LISA passband. The leading-order contribution to the inspiral phase enters at  $\mathcal{O}(\epsilon^{-1})$  and is driven by the adiabatic, first-order-in-the-mass-ratio, self-force  $F_{\text{ad}}^{(1)\alpha}$ . A number of authors have used  $F_{\text{ad}}^{(1)\alpha}$  to calculate the leading-order phase evolution of generic inspirals into Kerr black holes [19, 20, 68]. At subleading order (ignoring resonances that only affect generic inspirals into rotating black holes [44]) the next contributions to the orbital phase enter at  $\mathcal{O}(\epsilon^0)$ . These include the oscillatory part of the first-order force,  $F_{\text{osc}}^{(1)\alpha}$ , and the adiabatic part of the second-order force,  $F_{\text{ad}}^{(2)\alpha}$ .

In order to classify the effects of the secondary's spin in this hierarchy we must relate the spin magnitude to the mass ratio. If the secondary is a rotating black hole we can write

$$S \equiv |s|\mu^2, \quad \text{where } |s| \leq 1. \quad (2.5)$$

all other reasonable stellar objects have an even smaller spin—see e.g., Sec. II.B.1 of [69]. With this definition we can, by comparing the two terms in Eq. (2.1), conclude that the (conservative) MPD and the adiabatic part of the  $F_{\text{dipole}}^{(1)\alpha}$  will contribute to the orbital phase at subleading-order.

To summarize, the influence of each component of the force on the phase of the waveform in the inspiral is

$$\begin{aligned} \Phi = & \underbrace{\kappa_0 \epsilon^{-1}}_{\text{adiabatic: } F_{\text{ad}}^{(1)\alpha}} + \underbrace{\kappa_{1/2} \epsilon^{-1/2}}_{\text{resonances (Kerr only)}} + \underbrace{\kappa_1 \epsilon^0}_{\text{post-1-adiabatic: } F_{\text{osc}}^{(1)\alpha} + F_{\text{ad}}^{(2)\alpha}} + \dots, \end{aligned} \quad (2.6)$$

where the  $\kappa$  coefficients are dimensionless, of order unity, and depend on the ingress and egress (or merger) frequencies in a particular detector, but not on the mass ratio  $\epsilon$ .

### III. OVERVIEW OF OUR APPROACH

The MPD force is calculated by evaluating spin and curvature quantities at the instantaneous position of the smaller body. In contrast, the self-force is a functional of the smaller body's past worldline. To compute an inspiral in a self-consistent manner one solves for the worldline using Eq. (2.1) while simultaneously calculating the perturbation in the gravitational field to generate the local self-force [59]. In this work at each instance along the worldline we approximate the true (inspiraling) past worldline of the small body with the geodesic that is tangent at that instance. The tangent geodesic is periodic allowing the self-force to be computed efficiently in the frequency-domain. We use make of this approach to compute the self-force in the Lorenz gauge [57, 58, 70, 71].

This *geodesic self-force approximation* introduces a discrepancy with the true inspiral at post-1-adiabatic order [72], but preliminary evidence suggests that the coefficient of this error term is small [73–75].

Approximating the true self-force by the self-force calculated for motion along geodesics tangent to the worldline naturally suggests evolving the inspirals using a relativistic osculating elements prescription [76, 77]. These prescriptions recast of the equation of motion Eq. (2.1) (making no small force assumption) and describe the inspiral in terms of geometric quantities. The derivation in Schwarzschild spacetime by Pound and Poisson [76] is restricted to motion in the equatorial plane so in Sec. IV we extend it to generic motion required when the spin of the secondary and the orbital angular momentum are not aligned.

Second-order self-force results have not yet been computed. From Eq. (2.6) we see that neglecting  $F_{\text{ad}}^{(2)\alpha}$  introduces error at post-1-adiabatic order. Once second-order results are known they will be straightforward to incorporate into our scheme, but in this paper only first-order self-force effects are included. Similarly, there are dissipative effects from the spin of the secondary that enter at post-1-adiabatic order. These have been calculated for circular orbits in Schwarzschild [78] and Kerr [79, 80] spacetime, but to the best of our knowledge have not yet been calculated for eccentric orbits. Again, once  $F_{\text{dipole}}^{(1)\alpha}$  is known it can be straightforwardly incorporated into our long term evolution scheme. As we do not yet have calculations for these pieces of the force we will hereafter often adopt the notation

$$F_{\text{self}}^{\alpha} \equiv \mu^2 F_{\text{mono}}^{(1)\alpha}, \quad (3.1)$$

$$F_{\text{spin}}^{\alpha} \equiv \mu^2 s F_{\text{spin-curvature}}^{\alpha}. \quad (3.2)$$

Finally, from Eq. (2.6), we note that the adiabatic self-force enters at lower order than the other components of the force, and accordingly must be computed with greater accuracy in order to affect the phase error at the same level. To ensure the self-force is sufficiently accurate we use a hybrid scheme that computes the adiabatic component of the self-force with a highly accurate Regge-Wheeler code and computes the other components with a Lorenz-gauge code. This scheme is detailed in previous papers [58, 71].

### IV. OSCULATING ELEMENT DESCRIPTION OF MOTION

In this section we recast the equations of motion (2.1) into ones for the evolution of the osculating elements of the inspiral. This procedure is analogous to Lagrange's equations of planetary motion in Newtonian celestial mechanics. Relativistic osculating element prescriptions of motion were first given for Schwarzschild spacetime by Pound and Poisson [76]. In that work they specialized to motion in the equatorial plane and here we generalize

their result to generic motion to allow for a description of the inspiral when the spin of the secondary is not aligned or anti-aligned with the orbital angular momentum. In deriving the osculating equations of motion we do not make any small force approximation or other assumptions about the forcing terms—those are independent assumptions that we will discuss in the next section. In describing the motion of the secondary we will treat it as a point particle, with discussion in the next section on the justification for this. We will parameterize the particle's motion by its proper time  $\tau$  and distinguish the particle's time-dependent coordinate location from general spacetime coordinates with a subscript 'p'.

The central idea to the osculating elements prescription arises from noting that at each point along the accelerated worldline,  $z^\mu(\tau)$ , there is a one-to-one relation between the particle's position and velocity and a tangent (or osculating) geodesic. Each tangent geodesic has associated with it a set of orbital elements  $I^A$  (such as energy, angular momentum, azimuthal angle at periastron, etc) that uniquely identifies the geodesic. Consequently the worldline can be described either by a sequence of spacetime coordinates,  $z^\mu(\tau)$ , or as a sequence of orbital elements of the osculating geodesics,  $I^A(\tau)$ . With the four-velocity of the tangent geodesic given by  $u_G^\alpha(I^A, \tau) = \partial_\tau z_G^\alpha(I^A, \tau)$ , we can write

$$z^\alpha(\tau) = z_G^\alpha(I^A, \tau), \quad u^\alpha(\tau) = u_G^\alpha(I^A, \tau), \quad (4.1)$$

where hereafter a sub/superscript 'G' denotes a quantity related to a geodesic. The equations of motion take the following form in terms of the osculating elements [76]

$$\frac{\partial z_G^\alpha}{\partial I^A} \frac{\partial I^A}{\partial \tau} = 0, \quad \mu \frac{\partial u_G^\alpha}{\partial I^A} \frac{\partial I^A}{\partial \tau} = F^\alpha. \quad (4.2)$$

Our explicit choice of osculating elements  $I^A$  for bound motion and the resulting equations of motion are given in the following subsections.

### A. Bound geodesics in Schwarzschild spacetime

During the adiabatic stages of an inspiral (before the particle plunges into the black hole) the geodesics tangent to the inspiral are bound and generically eccentric. In this section we describe these tangent geodesics. We begin by examining the case where the motion is confined to the equatorial plane. Later, we will generalize to inclined geodesics (though ones that are still confined to some plane, as must occur in the Schwarzschild background). We denote equatorial geodesics by a set of functions  $z_G^\alpha(\tau) = [t_p'(\tau), r_p'(\tau), \pi/2, \varphi_p'(\tau)]$ , parameterized by proper time  $\tau$ . For later convenience we will omit the 'prime' from coordinates that are invariant under rotations, i.e.,  $t_p = t_p'$  and  $r_p = r_p'$ . The geodesic four-velocity  $u_G^\alpha$  is given by

$$u_G^\alpha = \left( \frac{\mathcal{E}^G}{f_p}, u_G^r, 0, \frac{\mathcal{L}^G}{r_p^2} \right), \quad (4.3)$$

where  $f_p \equiv 1 - 2M/r_p$ , and  $\mathcal{E}^G$  and  $\mathcal{L}^G$  are the specific orbital energy and angular momentum, respectively. The constraint  $u^\alpha u_\alpha = -1$  yields an expression for  $u_G^r$ :

$$(u_G^r)^2 = (\mathcal{E}^G)^2 - f_p \left( 1 + \frac{(\mathcal{L}^G)^2}{r_p^2} \right). \quad (4.4)$$

We parameterize the geodesic with the orbital eccentricity,  $e$ , and semi-latus rectum,  $p$ , which are related to the radial turning points  $r_{\min}$  and  $r_{\max}$  via

$$p = \frac{2r_{\max}r_{\min}}{M(r_{\max} + r_{\min})}, \quad e = \frac{r_{\max} - r_{\min}}{r_{\max} + r_{\min}}. \quad (4.5)$$

Eq. (4.5) and the roots of Eq. (4.4) give the relationship between  $(p, e)$  and  $(\mathcal{E}, \mathcal{L})$ :

$$\mathcal{E}^G = \sqrt{\frac{(p-2)^2 - 4e^2}{p(p-3-e^2)}}, \quad \mathcal{L}^G = \frac{pM}{\sqrt{p-3-e^2}}. \quad (4.6)$$

Bound orbits exist with  $e < 1$  and  $p > 6 + 2e$ . For  $e < 1$  the line  $p = 6 + 2e$  is a separatrix between bound and plunging orbits [81].

In self-force calculations it is convenient to reparameterize the orbital motion (i.e., all the curve functions) with the relativistic anomaly  $\chi$  [82], defined so that

$$r_p(\chi) = \frac{pM}{1 + e \cos[\chi - \chi_0]}. \quad (4.7)$$

The parameter  $\chi_0$  specifies the value of  $\chi$  at periastron passage.

Eq. (4.7) can be used with Eqs. (4.3) and (4.6) to derive the following initial value equations for the evolution of the orbit

$$\frac{d\tau_p}{d\chi} = \frac{Mp^{3/2}}{(1 + e \cos v)^2} \sqrt{\frac{p-3-e^2}{p-6-2e \cos v}}, \quad (4.8)$$

$$\frac{dt_p}{d\chi} = \frac{r_p^2}{M(p-2-2e \cos v)} \sqrt{\frac{(p-2)^2 - 4e^2}{p-6-2e \cos v}}, \quad (4.9)$$

$$\frac{d\varphi_p'}{d\chi} = \sqrt{\frac{p}{p-6-2e \cos v}}, \quad (4.10)$$

where  $v \equiv \chi - \chi_0$ . It is useful to introduce initial values  $T$  and  $\Phi$  to Eqs. (4.9) and (4.10) respectively

$$t_p(\chi) = T + \int_{\chi_0}^{\chi - \chi_0} \frac{dt_p}{d\chi} dv, \quad (4.11)$$

$$\varphi_p'(\chi) = \Phi + \int_{\chi_0}^{\chi - \chi_0} \frac{d\varphi_p'}{d\chi} dv. \quad (4.12)$$

These integrals have analytic solutions in terms of special functions [83], and we find the analytic solution for  $\varphi_p'$  to be useful in this work

$$\varphi_p'(\chi) = \Phi + 2\sqrt{\frac{p}{p-6-2e}} \bar{F} \left( \frac{v}{2} \middle| \frac{-4e}{p-6-2e} \right), \quad (4.13)$$

where  $\bar{F}$  is the incomplete elliptic integral of the first kind

$$\bar{F}(a|b) \equiv \int_0^a (1 - b \sin^2 x)^{-1/2} dx. \quad (4.14)$$

We also find use for the incomplete elliptic integral of the second kind  $\bar{E}$

$$\bar{E}(a|b) \equiv \int_0^a (1 - b \sin^2 x)^{1/2} dx. \quad (4.15)$$

In a coordinate system where the geodesic appears inclined, the worldline is given by  $z_G^\alpha = [t_p(\tau), r_p(\tau), \theta_p(\tau), \varphi_p(\tau)]$ . To transform from  $z_G^\alpha$  to  $z_G^\alpha$  we will introduce a rotation matrix with Euler angles  $\Omega$  and  $\iota$

$$\begin{bmatrix} x_p \\ y_p \\ z_p \end{bmatrix} = \begin{bmatrix} \cos \Omega & -\sin \Omega \cos \iota & \sin \Omega \sin \iota \\ \sin \Omega & \cos \Omega \cos \iota & -\cos \Omega \sin \iota \\ 0 & \sin \iota & \cos \iota \end{bmatrix} \begin{bmatrix} x'_p \\ y'_p \\ z'_p \end{bmatrix}. \quad (4.16)$$

Here  $\Omega$  is the longitude of the ascending node and  $\iota$  is the orbital inclination. Using  $(x'_p, y'_p, z'_p) = (r_p \cos \varphi'_p, r_p \sin \varphi'_p, 0)$  the following equations are derived

$$x_p = r_p (\cos \Omega \cos \varphi'_p - \sin \Omega \cos \iota \sin \varphi'_p), \quad (4.17)$$

$$y_p = r_p (\sin \Omega \cos \varphi'_p + \cos \Omega \cos \iota \sin \varphi'_p), \quad (4.18)$$

$$z_p = r_p \sin \iota \sin \varphi'_p, \quad (4.19)$$

$$\phi \equiv \int_0^{\varphi'_p} (\sec \iota \cos^2 u + \cos \iota \sin^2 u)^{-1} du, \quad (4.20)$$

$$\varphi_p = \phi + \Omega, \quad (4.21)$$

$$\theta_p = \cos^{-1}(\sin \iota \sin \varphi'_p). \quad (4.22)$$

The  $\theta$  and  $\varphi$  components of  $u_G^\alpha$  are given by

$$u_G^\theta = -\frac{(1 + e \cos v)^2 \sin \iota \cos \varphi'_p}{pM \sqrt{(p-3-e^2)(1-\sin^2 \iota \sin^2 \varphi'_p)}}, \quad (4.23)$$

$$u_G^\varphi = \frac{(1 + e \cos v)^2 (p-3-e^2)^{-1/2}}{pM (\sec \iota \cos^2 \varphi'_p + \cos \iota \sin^2 \varphi'_p)}. \quad (4.24)$$

The  $u_G^t$  and  $u_G^r$  four-velocity components are unaffected by the rotation.

## B. Evolution of the orbital elements

The complete set of orbital elements we choose to describe the tangent geodesics are given by

$$I^A = \{e, p, \chi_0, \iota, \Omega, \Phi, T\}. \quad (4.25)$$

Any fixed set of these elements uniquely specifies a bound, eccentric, possibly inclined, geodesic in the space-time. To describe the inspiraling worldline we promote

these elements to have time-dependence. The rate-of-change of  $I^A$  is described by Eq. (4.2). In order to explicitly give the evolution equations, let us define the operator

$$\mathcal{D} \equiv \frac{de}{d\chi} \frac{\partial}{\partial e} + \frac{dp}{d\chi} \frac{\partial}{\partial p} + \frac{d\chi_0}{d\chi} \frac{\partial}{\partial \chi_0}, \quad (4.26)$$

Parameterizing the elements using  $\chi$  we can then write

$$0 = \mathcal{D}[t_p] + \frac{\partial t_p}{\partial T} \frac{dT}{d\chi}, \quad (4.27)$$

$$0 = \mathcal{D}[r_p], \quad (4.28)$$

$$0 = \mathcal{D}[\theta_p] + \frac{\partial \theta_p}{\partial \iota} \frac{d\iota}{d\chi} + \frac{\partial \theta_p}{\partial \Phi} \frac{d\Phi}{d\chi}, \quad (4.29)$$

$$0 = \mathcal{D}[\varphi_p] + \frac{\partial \varphi_p}{\partial \iota} \frac{d\iota}{d\chi} + \frac{\partial \varphi_p}{\partial \Omega} \frac{d\Omega}{d\chi} + \frac{\partial \varphi_p}{\partial \Phi} \frac{d\Phi}{d\chi}, \quad (4.30)$$

$$\frac{1}{\mu} \frac{d\tau_p}{d\chi} F^\alpha = \mathcal{D}[u_G^\alpha] \quad \text{where } \alpha = \{t, r\}, \quad (4.31)$$

$$\frac{1}{\mu} \frac{d\tau_p}{d\chi} F^\beta = \mathcal{D}[u_G^\beta] + \frac{\partial u_G^\beta}{\partial \iota} \frac{d\iota}{d\chi} + \frac{\partial u_G^\beta}{\partial \Phi} \frac{d\Phi}{d\chi} \quad \text{where } \beta = \{\theta, \varphi\}, \quad (4.32)$$

Eqs. (4.28) and (4.31) form a closed system that describes the evolution of the elements  $\alpha = \{e, p, \chi_0\}$

$$\frac{d\alpha}{d\chi} = c_\alpha^{(t)} F^t + c_\alpha^{(r)} F^r, \quad (4.33)$$

The  $c$ -coefficients depend on  $e$ ,  $p$ , and  $v$  and, as they are a little unwieldy, are given explicitly in Appendix A.

To take advantage of our hybrid self-force technique [58, 71] we eliminate  $F^r$  from the  $\alpha = \{p, e\}$  versions of Eq. (4.33) using the orthogonality condition  $u_\mu F^\mu = 0$

$$F^r = \frac{f_p (f_p u^t F^t - r_p^2 u^\theta F^\theta - r_p^2 \sin^2 \theta_p u^\varphi F^\varphi)}{u^r}. \quad (4.34)$$

This form appears inconvenient because  $u^r$  vanishes at the radial turning points. However, the presence of a  $\sin v$  factor in Eqs. (A2) and (A4) allows the resulting expressions to be simplified in such a way that the denominator does not vanish. Eq. (4.27) describes the rate-of-change of  $T$ . However, instead of calculating  $T$  we dynamically evolve  $t_p$  using Eq. (4.9). Eq. (4.29) and (4.32) describe the evolution of the elements  $\alpha = \{\iota, \Phi\}$

$$\frac{d\alpha}{d\chi} = c_\alpha^{(\theta)} F^\theta + c_\alpha^{(e)} \frac{de}{d\chi} + c_\alpha^{(p)} \frac{dp}{d\chi} + c_\alpha^{(\chi_0)} \frac{d\chi_0}{d\chi}, \quad (4.35)$$

Similarly, Eq. (4.30) describes the evolution of  $\Omega$

$$\frac{d\Omega}{d\chi} = c_\Omega^{(e)} \frac{de}{d\chi} + c_\Omega^{(p)} \frac{dp}{d\chi} + c_\Omega^{(\chi_0)} \frac{d\chi_0}{d\chi} + c_\Omega^{(\iota)} \frac{d\iota}{d\chi} + c_\Omega^{(\Phi)} \frac{d\Phi}{d\chi}. \quad (4.36)$$

The  $c$ -coefficients in these two equations depend on  $e$ ,  $p$ ,  $v$ ,  $\iota$ , and  $\varphi'_p$  and their explicit form can be found in

Appendix A. Note that in the  $c_{\Phi}^{(\theta)}$  coefficient given in Eq. (A11) there is a  $1/\sin \iota$  factor that diverges when  $\iota = 0$ . This is a familiar property of osculating orbits in Newtonian celestial mechanics. To circumvent this issue one can change to a different set of orbital elements or, as we do in this work, leverage the spherical symmetry of the problem. Without loss of generality, we choose the initial condition  $\iota_0 = \pi/4$  which avoids the worldline ever crossing  $\iota = \{0, \pi/2\}$  as under our small mass-ratio approximation  $\iota$  will oscillate with a small amplitude.

## V. FORCING TERMS

The forcing terms that drive the inspiral are on the righthand side of Eq. (2.1). In this work we do not include the second-order or spin-dipole forcing terms (as they have yet to be calculated) so the force,  $F^\mu$ , has two parts

$$F^\alpha = \mu^2 \left( F_{\text{mono}}^{(1)\alpha} + s F_{\text{spin-curvature}}^\alpha \right) = F_{\text{self}}^\alpha + F_{\text{spin}}^\alpha. \quad (5.1)$$

The first term arises from the interaction of the secondary with its own (first-order in the mass-ratio) metric perturbation and is known as the (first-order) self-force. The second term arises from the interaction of the spin of the secondary with the background spacetime of the primary. This force is known as the Mathisson-Papapetrou-Dixon (MPD) spin-curvature force. We discuss how these two forcing terms are calculated in the following subsections.

### A. Self-force

In the small mass ratio limit the spacetime metric of the binary can be written as  $g_{\mu\nu} + h_{\mu\nu}$  where  $g_{\mu\nu}$  is the background metric of the primary and  $h_{\mu\nu}$  is a first-order-in-the-mass-ratio perturbation arising from the secondary (we do not include higher-order in the mass ratio corrections in this work). Within this description the secondary interacts with its own metric perturbation. This self-interaction gives rise to a self-force that acts to drive the inspiral. Being sourced by the metric perturbation backscattering off the background curvature of the primary, this self-interaction is non-local so that the self-force at any instance is a functional of the the entire past (inspiraling) history of the secondary. This makes the self-force particularly challenging to calculate.

One way to make the calculation more amenable is to restrict the secondary's motion to a geodesic of the background spacetime. The periodic nature of the geodesic then allows efficient frequency-domain techniques to be employed [57, 58, 70, 71, 84–91] and we make use of this approach in this work. Approximating the true self-force at each instance (a functional of the inspiraling worldline) with the geodesic self-force introduces a discrepancy with the true inspiral at post-1-adiabatic order [72], but preliminary evidence suggests that the coefficient of this

error term is very small [73–75]. When the spin of the secondary is not aligned with the orbital angular momentum the orbit will precess about the initial equatorial plane. The effect of this precession on the self-force is captured by the  $F_{\text{dipole}}^{(1)\alpha}$  term that we are not currently including in our model (but once it has been calculated it is straightforward to incorporate).

We now briefly review our calculation of the self-force. We model the secondary as a point particle to give an unambiguous result that does not depend on the higher multipole structure of the body (though we will add dipole structure to account for the body's spin in the next subsection). This point particle model necessitates a regularization procedure to handle the divergence in the metric perturbation at the particle's location [22, 92, 93]. Practically, we make use of the mode-sum scheme [94–100]. The regularization procedure was, until recently [101], only understood in the Lorenz gauge. In this gauge the trace-reversed metric perturbation,  $\bar{h}_{\mu\nu} \equiv h_{\mu\nu} - \frac{1}{2}g_{\mu\nu}(h_{\alpha\beta}g^{\alpha\beta})$ , is governed by the linearized Einstein equations subject to the constraint  $\nabla^\mu \bar{h}_{\mu\nu} = 0$

$$\square \bar{h}_{\mu\nu} + 2R^\alpha{}_{\mu}{}^\beta{}_{\nu} \bar{h}^{\alpha\beta} = -16\pi T_{\mu\nu}, \quad (5.2)$$

where  $\square \equiv g^{\alpha\beta} \nabla_\alpha \nabla_\beta$ ,  $R^\alpha{}_{\mu}{}^\beta{}_{\nu}$  is the Riemann tensor of the background spacetime, and  $T_{\mu\nu}$  is the stress energy tensor of a point mass following a geodesic. A number of authors have considered Lorenz-gauge metric perturbations in Schwarzschild spacetime [57, 70, 71, 84–87, 89–91, 102, 103] and Kerr spacetime [32]. This work utilizes the frequency domain code presented in Ref. [71] with refinements described in Refs. [58, 91].

The adiabatic part of the self-force, which contributes at leading-order in Eq. (2.6), must be calculated to within an error tolerance smaller than the mass ratio whereas the terms contributing at post-1-adiabatic order require only a few digits of accuracy. We use a hybrid scheme [58, 71] that has been developed to achieve these tolerances. This hybrid scheme uses a highly accurate Regge-Wheeler-Zerilli (RWZ) [104, 105] code (based on Refs. [88, 91]) to generate  $F_{\text{ad}}^\mu$  while post-processing the Lorenz gauge self-force (and spin-curvature force) results to calculate  $F_{\text{osc}}^\mu$ . This scheme relaxes the requirements on our Lorenz-gauge self-force code (which takes substantially longer to run than the RWZ code at high precision) while maintaining target phase accuracies in the resulting inspiral.

Our hybrid code outputs the Fourier coefficients of the self force for a given orbital configuration. We calculate these Fourier coefficients for tens of thousands of orbital configurations and perform an interpolation over the relevant parameter space. We minimize interpolation error by performing multiple local interpolations, modifying our discretization in regions where the self-force varies more rapidly e.g., near the separatrix. For full details see Ref. [58]. This interpolant can be rapidly evaluated for any orbit configuration (including those not in the

original dataset) and we couple the interpolant with the osculating element equations of motion to compute inspirals.

Our hybrid code computes the self-force in a coordinate system where the instantaneous orbital motion is equatorial (the ‘prime’ coordinate system). In this coordinate system  $F_{\text{self}}^{\theta}$  vanishes. To transform to the inclined frame we apply a rotation giving

$$F_{\text{self}}^t = F_{\text{self}}^{\prime t}, \quad F_{\text{self}}^r = F_{\text{self}}^{\prime r}, \quad (5.3)$$

$$F_{\text{self}}^{\theta} = -\frac{4 F_{\text{self}}^{\prime \varphi} \sin \iota \cos \varphi'_p \sqrt{1 - \sin^2 \iota \sin^2 \varphi'_p}}{3 + \cos(2\iota) + 2 \cos(2\varphi'_p) \sin^2 \iota}, \quad (5.4)$$

$$F_{\text{self}}^{\varphi} = \frac{4 F_{\text{self}}^{\prime \varphi} \cos \iota}{3 + \cos(2\iota) + 2 \cos(2\varphi'_p) \sin^2 \iota}. \quad (5.5)$$

## B. Spin-curvature force

When multipole-moments beyond the monopole are endowed to the orbiting particle there is an interaction between them and the Riemann tensor of the background spacetime. Ignoring the self-force and multipole-moments beyond the spin of the body (the ‘pole-dipole’ approximation) gives rise to the Mathisson-Papapetrou-Dixon equations of motion [63, 64, 106]

$$u^{\beta} \nabla_{\beta} p^{\alpha} = -\frac{1}{2} R^{\alpha}_{\nu\lambda\sigma} u^{\nu} S^{\lambda\sigma} \quad (5.6)$$

$$u^{\beta} \nabla_{\beta} S^{\mu\nu} = p^{\mu} u^{\nu} - p^{\nu} u^{\mu}. \quad (5.7)$$

where  $p^{\alpha}$  is the particle’s four-momentum and  $S^{\alpha\beta}$  is the spin tensor of the orbiting body. Generically, the four-velocity and the four-momentum are not aligned, i.e.,  $p^{\alpha} \neq \mu u^{\alpha}$ .

The systems of equations (5.6) and (5.7) do not form a closed system and an additional spin-supplementary condition (SSC) must be imposed. The choice of SSC is not unique owing to the fact that in relativity the center of mass of a spinning body is an observer dependent point. The choice of SSC is fundamentally arbitrary but might be motivated by simplifying the equations of motion for a particular setup. Careful comparison shows that each SSC leads to the same physics [107–109]. In this work we adopt the Pirani condition [110]

$$u_{\mu} S^{\mu\nu} = 0. \quad (5.8)$$

It is convenient to introduce the spin vector,  $S^{\mu}$ , from which the spin tensor can be constructed

$$S^{\mu\nu} = \epsilon^{\mu\nu\alpha\beta} u_{\alpha} S_{\beta}, \quad (5.9)$$

where  $\epsilon^{\mu\nu\alpha\beta}$  is the Levi-Civita tensor. The magnitude of the spin vector  $S^2 \equiv S^{\alpha} S_{\alpha}$  is a constant [111].

The set of equations (5.6), (5.7) and (5.8) can be integrated to compute the worldline of a spinning body.

For each Killing vector  $\xi_{(j)}^{\alpha}$  of the spacetime the quantity [111]

$$\mathcal{C}^S = p_{\alpha} \xi_{(j)}^{\alpha} - \frac{1}{2\mu} S^{\alpha\beta} \nabla_{\beta} \xi_{\alpha}^{(j)}. \quad (5.10)$$

is conserved along the body’s worldline. The first term of Eq. (5.10) is conserved for a geodesic (e.g.  $\mu \mathcal{E}^G = p_{\alpha} \xi_{(t)}^{\alpha}$ ) while the second term accounts for the MPD force. Here a superscript  $S$  denotes a conserved quantity related to a spinning body (recall that a superscript  $G$  denotes a quantity conserved for a geodesic). The four Killing vectors of Schwarzschild spacetime admit four conserved quantities in accordance with Eq. (5.10). We demonstrate conservation of two of these quantities as a consistency check in Section VIII A by disabling (for testing purposes) the self-force in our numerical scheme.

As we are working in the small mass-ratio limit  $\epsilon \ll 1$  Eq. (2.5) tells us that the spin magnitude is also small. We thus linearize our calculation in  $S$ . This results in substantially simpler equations of motion, though it is an open question whether the non-linear (in  $S$ ) terms might lead to interesting resonance phenomenon that the linear approximation does not capture [111]. To linear order in  $S$  the four-velocity and angular-momentum are parallel

$$u^{\alpha} = p^{\alpha} / \mu + \mathcal{O}(S^2). \quad (5.11)$$

The equations of motion (5.6)-(5.7) reduce to

$$u^{\beta} \nabla_{\beta} u^{\alpha} = -\frac{1}{2} R^{\alpha}_{\nu\lambda\sigma} u^{\nu} S^{\lambda\sigma} \quad (5.12)$$

$$u^{\beta} \nabla_{\beta} S^{\mu\nu} = 0. \quad (5.13)$$

Comparing Eq. (2.1) and Eq. (5.12) we identify the spin-curvature force as

$$F_{\text{spin}}^{\alpha} = -\frac{1}{2} R^{\alpha}_{\nu\lambda\sigma} u^{\nu} S^{\lambda\sigma} \quad (5.14)$$

Equation (5.13) tells us that, to linear order in  $S$ , the spin vector is parallel transported along the worldline. In Schwarzschild spacetime this gives us explicitly

$$\frac{dS^{\alpha}}{d\tau} = -\Gamma^{\alpha}_{\mu\nu} S^{\mu} u^{\nu}, \quad (5.15)$$

$$\frac{dS^t}{d\chi} = -\frac{d\tau_p}{d\chi} \frac{M}{f_p r_p^2} (S^t u^r + S^r u^t), \quad (5.16)$$

$$\begin{aligned} \frac{dS^r}{d\chi} = \frac{d\tau_p}{d\chi} \left( \frac{M}{f_p r_p^2} (S^r u^r - f_p^2 S^t u^t) \right. \\ \left. + f_p r_p (S^{\theta} u^{\theta} + S^{\varphi} u^{\varphi} \sin^2 \theta_p) \right), \end{aligned} \quad (5.17)$$

$$\frac{dS^{\theta}}{d\chi} = \frac{d\tau_p}{d\chi} \left( S^{\varphi} u^{\varphi} \cos \theta_p \sin \theta_p - \frac{S^{\theta} u^r + S^r u^{\theta}}{r_p} \right), \quad (5.18)$$

$$\frac{dS^{\varphi}}{d\chi} = -\frac{d\tau_p}{d\chi} \left( \frac{\cos \theta_p}{\sin \theta_p} (S^{\varphi} u^{\theta} + S^{\theta} u^{\varphi}) + \frac{S^r u^{\varphi} + S^{\varphi} u^r}{r_p} \right). \quad (5.19)$$

To couple these spin evolution equations to the osculating elements equations we rewrite them as forcing terms. Eqs. (5.8) and (5.9) imply that the spin vector is purely spatial in the rest frame of the small body

$$u_\mu S^\mu = 0. \quad (5.20)$$

We use this condition to determine  $S^t$

$$S^t = \frac{S^r u^r + f_p r_p^2 (S^\theta u^\theta + S^\varphi u^\varphi \sin^2 \theta_p)}{f_p^2 u^t}. \quad (5.21)$$

This leaves three degrees of freedom for choosing the initial conditions of  $S^\mu$ . Using Eq. (5.14) and (5.9) to express the components of  $F_{\text{spin}}^\mu$  in terms of the components of the spin vector gives

$$F_{\text{spin}}^t = \frac{3M u^r \sin \theta_p (S^\varphi u^\theta - S^\theta u^\varphi)}{r_p f_p}, \quad (5.22)$$

$$F_{\text{spin}}^r = \frac{3M f_p u^t \sin \theta_p (S^\varphi u^\theta - S^\theta u^\varphi)}{r_p}, \quad (5.23)$$

$$F_{\text{spin}}^\theta = \frac{3M u^\varphi \sin \theta_p (S^t u^r - S^r u^t)}{r_p^3}, \quad (5.24)$$

$$F_{\text{spin}}^\varphi = -\frac{3M u^\theta (S^t u^r - S^r u^t)}{r_p^3 \sin \theta_p}. \quad (5.25)$$

## VI. WAVEFORMS

Coupling the force terms in the previous section with the osculating element equations of motion in Sec. IV allows for the computation of inspiral trajectories. With a trajectory in hand there are a number of ways to compute the waveform.

The most accurate method is to use the trajectory as a source in a time-domain code. Via extrapolation or via hyperboloidal compactification, the waveform can be extracted at null infinity [59, 112, 113]. The high computational cost of these time-domain simulations means they cannot provide a wide survey of waveforms across the parameter space but they are invaluable to assess the accuracy of other waveform generation methods.

One of the most common methods for computing waveforms is to use the weak-field quadrupole formula (sometimes supplemented by octupolar or fast-motion corrections). This technique is taken by so-called ‘kludge’ methods [20, 114, 115] that combine input from a number of different techniques (e.g., post-Newtonian and black hole perturbation theory) to model the trajectory. These techniques allow waveforms to be computed rapidly but they may not faithfully represent the true waveform in the very strong-field [20].

In this work we take a different approach inspired by our geodesic self-force interpolation model. Using our frequency-domain codes we compute so-called ‘snapshot’ waveforms [19, 68] for a large number of parameters in the  $(p, e)$  space. We then interpolate between these snapshot waveforms to create a continuously evolving waveform over the entire inspiral.

### A. Frequency-domain waveforms

The radiation from the binary can be extracted from the (complex) Weyl curvature scalar

$$\Psi_4 = -C_{\alpha\beta\gamma\delta} n^\alpha \bar{m}^\beta n^\gamma \bar{m}^\delta \quad (6.1)$$

where  $C_{\alpha\beta\gamma\delta}$  is the Weyl curvature tensor (equal to the Riemann tensor in vacuum), and  $n^\alpha$  and  $\bar{m}^\alpha$  are components of the Kinnersly tetrad [116]. Far from the source  $\Psi_4$  can be related to the gravitational radiation via

$$\Psi_4(r \rightarrow \infty) \simeq \frac{1}{2} (\ddot{h}_+ - i\ddot{h}_\times). \quad (6.2)$$

where  $h_+$  and  $h_\times$  are the two independent polarizations of the gravitational waves and an overdot denotes differentiation with respect to coordinate time.

The scalar  $\Psi_4$  can be decomposed into spin-weighted spherical harmonics  ${}_{-2}Y_{lm}$  as

$$\Psi_4(t, r, \theta, \varphi) = \sum_{l=2}^{l_{\max}} \sum_{m=-l}^l \psi_4^{lm}(t, r) {}_{-2}Y_{lm}(\theta, \varphi). \quad (6.3)$$

The function  $\psi_4$  can be obtained directly using the Teukolsky formalism [116]. As our hybrid self-force scheme employs highly accurate results in the Regge-Wheeler gauge we already have precomputed data for the asymptotic amplitudes of the RWZ fields. These amplitudes can be related to  $\psi_4$  via

$$\begin{aligned} \psi_4^{lm}(r \rightarrow \infty) \simeq & \sum_{n=n_{\min}}^{n_{\max}} \frac{\omega_{mn}^2}{4r} \sqrt{(l+2)(l+1)l(l-1)} \\ & \times (iC_{lmn}^{\text{odd}} - C_{lmn}^{\text{even}}) e^{-i\omega_{mn}(t-r)}, \end{aligned} \quad (6.4)$$

where  $C_{lmn}^{\text{even}}$  is the coefficient of the Zerilli-Moncrief master function [105, 117], and  $C_{lmn}^{\text{odd}}$  is the coefficient of the Cunningham-Price-Moncrief master function [118, 119] (according to the conventions of [88]) and  $\omega_{mn} = m\Omega_\varphi + n\Omega_r$  is the mode frequency. The waveform is calculated by integrating Eq. (6.2) twice with respect to time, giving

$$\begin{aligned} h_+ - ih_\times = & \frac{1}{r} \sum_{l=2}^{l_{\max}} \sum_{m=-l}^l H_{lm}(t, r) {}_{-2}Y_{lm}(\theta, \varphi), \quad (6.5) \\ H_{lm}(t, r) \equiv & \sum_{n=n_{\min}}^{n_{\max}} \frac{1}{2} \sqrt{(l+2)(l+1)l(l-1)} \\ & \times (C_{lmn}^{\text{even}} - iC_{lmn}^{\text{odd}}) e^{-i\omega_{mn}(t-r)}, \end{aligned} \quad (6.6)$$

In order to evaluate  $C_{lmn}^{\text{even/odd}}$  for arbitrary values of  $(p, e)$  we interpolate over the parameter space using the same scheme that we used for the self-force [58]. In total we computed 11,234 orbital configurations in the range  $p < 57$  and  $e < 0.82$ . For purposes of reconstructing waveforms, the  $C$ -coefficients are interpolated for a range of indices:  $n_{\min} = -40$  through  $n_{\max} = +40$ , and for every  $m$  for  $l = 2$  and  $l = 3$ .

Using this prescription the waveform for a given  $(p, e)$ , corresponds to a geodesic with periastron passage at  $t = \varphi = 0$ . To compute the waveform associated with an inspiral we update the snapshot parameters  $(p, e, t, \varphi)$  at each periastron passage to maintain consistency between the inspiraling orbital motion and the waveform's amplitude and phase. The values of  $(p, e)$  jump discontinuously at periastron passages under this method. This jump has a minimal effect on our inspiral waveform, as the dephasing between the geodesic waveform and the true inspiral waveform takes places over the radiation reaction timescale which is much longer than the orbital timescale. These discontinuous changes will thus be negligible for small mass-ratio binaries while the inspiral is evolving adiabatically (as it does away from the separatrix). As the waveform and inspiral parameters are synchronized at each periastron passage our inspiral waveform should be a good representation of the true waveform throughout the entire adiabatic inspiral.

## VII. SPIN-ALIGNED INSPIRALS (PLANAR MOTION)

For orbits where the spin and orbital angular momentum are aligned the inspiral motion is confined to a plane. In this scenario the osculating elements equations simplify greatly ( $dt/d\chi = d\Omega/d\chi = 0$ ). When  $\iota$  and  $\Omega$  are constant the troublesome  $1/\sin \iota$  terms can be avoided by calculating  $\varphi'_p$  dynamically using Eq. (4.10) instead of evolving  $\Phi$ . Under these simplifications our osculating elements scheme is applied to equatorial inspirals by enforcing the condition  $\iota = 0$  or, equivalently,  $\theta_p = \pi/2$ . In this case the only non-zero component of the spin vector,  $S^\alpha$ , is

$$S^\theta = \frac{s\mu^2}{r_p}. \quad (7.1)$$

Consequently, from Eqs. (5.22)-(5.25), only  $F_{\text{spin}}^t$  and  $F_{\text{spin}}^r$  are non-zero

$$F_{\text{spin}}^t = -\frac{3s\mu^2 M u^r u^\varphi}{r_p^2 f_p} \quad (7.2)$$

$$F_{\text{spin}}^r = -\frac{3s\mu^2 M f_p u^t u^\varphi}{r_p^2}. \quad (7.3)$$

We now present some sample inspirals and waveforms for the spin-aligned case.

### A. Sample results

It is key to assess how a spinning secondary influences the phasing of the inspiral. We compare the inspiral phase for binaries with a spinning secondary against non-spinning binaries and show the results for the inspiral trajectories in Figs. 1 and 2 and sample waveforms in

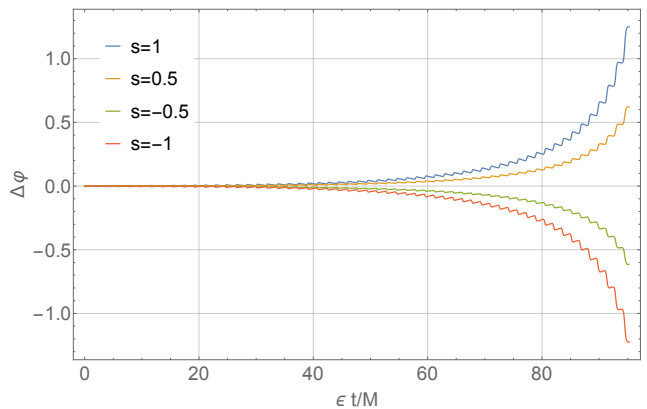


FIG. 1. Dephasing of inspirals with a spinning secondary with respect to a non-spinning inspiral. The dephasing is defined as  $\Delta\varphi \equiv \varphi_p^{s \neq 0} - \varphi_p^{s=0}$ . The initial parameters for the non-spinning inspiral are  $(p_0, e_0) = (10, 0.4)$  and the initial frequencies of the spinning inspirals are matched to the initial frequencies of the non-spinning case. For these calculations we choose a mass ratio of  $\mu/M = 5 \times 10^{-3}$ , which is large enough that the eccentric oscillations of the inspirals are visible in the figure. Reading from top to bottom the spin values are  $s = \{+1, +0.5, -0.5, -1\}$ .

Figs. 3 and 4. When we compare inspirals we match the initial frequencies of the spinning inspiral with the frequencies of the non-spinning inspiral using the technique described in our previous paper [58].

For Fig. 1 the initial parameters for the non-spinning binary are  $(p, e) = (10, 0.4)$ . Over the course of the inspiral we find for the maximum spin  $|s| = 1$  that the orbit dephases by  $\Delta\varphi \sim 1.2$  radians. In this example spin-aligned binaries act to increase the phase of the inspiral with respect to the non-spinning case. Similarly, anti-aligned binaries act to decrease the inspiral phase. Burko and Khanna [62] consider a similar setup for the evolution of quasi-circular inspirals including spin-curvature effects. In their Fig. 6 they consider the effect of varying the spin on the secondary for inspirals which start at  $r_0 = 10M$ . In the quasi-circular case, they find  $\sim 4$  radians of phase difference for the  $|s| = 1$  inspiral. Our results and theirs cannot be directly compared, however, as they attempt to include second-order radiative effects (via a post-Newtonian approximation) in their inspiral calculation, which are not a part of our model.

The phase difference observed in the example presented in Fig. 1, whereby the spin-aligned binary takes longer to merge than the spin anti-aligned binary, is reminiscent of the ‘orbital hangup’ observed for circular binaries in numerical relativity simulations [120]. A more exhaustive search through the  $(p_0, e_0)$  parameter space reveals that this behavior is not universal and for some configurations the opposite is observed, i.e., a spin-aligned binary can accumulate less phase than the associated non-spinning binary. Figure 2 demonstrates this change in behaviour for a number of inspirals that differ in  $p_0$  but each begin with the same high initial eccen-

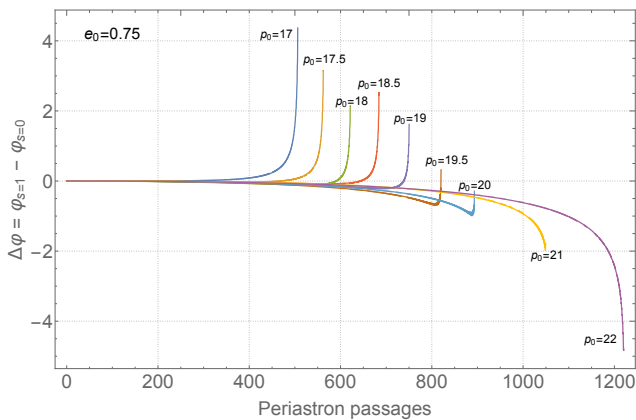


FIG. 2. Dephasing of a spin-aligned binary with respect to a (initially frequency matched) non-spinning binary. All inspirals initially have eccentricity  $e_0 = 0.75$  and we show  $\Delta\varphi = \varphi_{s=1} - \varphi_{s=0}$  for a variety of inspirals with differing initial  $p_0$  values. For inspirals with a strong-field  $p_0 \lesssim 19$  the accumulation of  $\Delta\varphi$  is positive and monotonic (modulo oscillations on the orbital timescale). For  $p_0 \gtrsim 21$  the accumulation of  $\Delta\varphi$  is negative and monotonic. Between these two regimes the accumulation of  $\Delta\varphi$  is not monotonic and the spinning inspiral can initially lose phase with respect to the non-spinning case before catching up again, even returning to being in phase ( $\Delta\varphi = 0$ ) as plunge is approached. The opposite behavior is observed for spin anti-aligned ( $s = -1$ ) binaries. The inspirals in this figure were computed with mass ratio  $\epsilon = 5 \times 10^{-3}$ .

tricity  $e_0 = 0.75$ . In general we find that spin-aligned inspirals with a  $p_0$  in the strong-field ( $p \lesssim 20$ ) accumulate more phase before the onset of the plunge than the non-spinning case, whereas spin-aligned inspirals with  $p_0$  in the weak field ( $p \gtrsim 20$ ) experience the opposite and accumulate less phase before the onset of the plunge than the non-spinning case. We also observe that the accumulation of the  $\Delta\varphi$  is not always monotonic, e.g., for  $p_0 \simeq 20$  a spin-aligned binary can initially lose phase with respect to the non-spinning case but can catch up with it later, even to the extent that the two inspirals realign in phase ( $\Delta\varphi = 0$ ). We observe this change of sign of  $\Delta\varphi$  occurs regardless of the initial eccentricity, including for quasi-circular inspirals with  $e_0 = 0$ .<sup>1</sup> For these inspirals we observe the change in sign of  $\Delta\varphi$  occurs for inspirals with  $p_0 \simeq 30$ .

The influence of the spin-curvature force on  $\Delta\varphi$  contrasts with that of the conservative self-force, which always acts to reduce the inspiral phase [25, 58]. In regions of the parameter space where the effect of the spin-

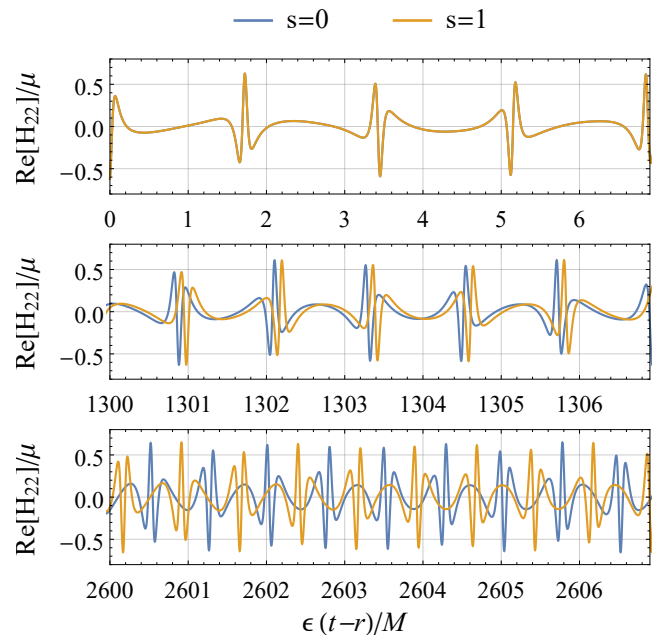


FIG. 3. Sample waveforms for inspirals with a spinning and non-spinning secondary with  $\epsilon = 10^{-3}$ . The initial orbital parameters are  $(p_0, e_0) = (20, 0.7)$ . We match the initial frequencies of the spinning and non-spinning configuration so that the two waveforms are initially in phase (top panel). After  $\sim 140$  radial oscillations the dephasing of the waveforms becomes noticeable (middle panel). After  $\sim 360$  radial oscillations the waveforms have dephased by a half cycle (bottom panel). Close to the plunge ( $\sim 700$  radial oscillations,  $\epsilon(t-r)/M \simeq 3700$ ) the waveforms have dephased by 2 complete cycles.

ning secondary acts to monotonically increase the inspiral phase this raises the possibility that waveforms associated with an inspiral computed using the radiative approximation [19, 68] plus a spinning secondary might closely mimic a waveform computed using the full dissipative and conservative self-force with a non-spinning binary. Exploring the possible degeneracies between these two models we leave for future work.

In Figs. 3 and 4 we show gravitational waveforms from a high and a medium eccentricity inspiral, respectively. Each figure contains three panels, displaying three different epochs in the inspiral. The figures show the waveforms at an early time, when the dephasing first becomes noticeable, and later when the waveforms first dephase by a half cycle. To display the dephasing, each panel shows the waveforms for both the spinning and non-spinning cases. Initially, the frequencies of the two waveforms are matched but over time the waveforms dephase by a number of cycles.

<sup>1</sup> In the literature it is common to read statements like ‘circular orbits remain circular as they adiabatically evolve due to radiation reaction’. This statement is true when one is concerned only with the leading-order phase evolution. When modeling post-1-adiabatic corrections, as in this work, it is important to note that inspirals with  $e_0 = 0$  develop eccentricity which oscillates near  $e = 0$  with an amplitude that scales with the mass ratio.

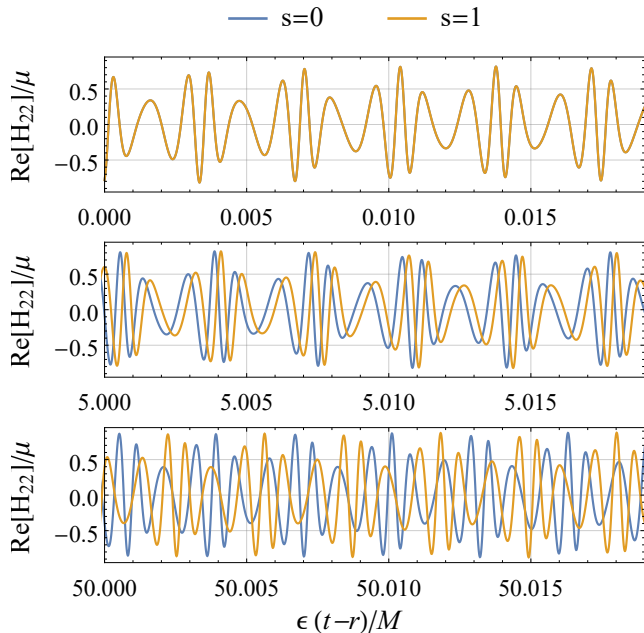


FIG. 4. Sample waveforms for inspirals with a spinning and non-spinning secondary with  $\epsilon = 10^{-5}$ . The initial orbital parameters are  $(p_0, e_0) = (10, 0.3)$ . We match the initial frequencies of the spinning and non-spinning configuration so that the two waveforms are initially in phase (top panel). After  $\sim 230$  radial oscillations the dephasing of the waveforms becomes noticeable (middle panel). After  $\sim 2400$  radial oscillations the waveforms have dephased by a half cycle (bottom panel). Close to the plunge ( $\sim 4400$  radial oscillations,  $\epsilon(t-r)/M \simeq 90$ ) the waveforms have dephased by 15 complete cycles.

### VIII. ARBITRARY SPIN INSPIRALS WITH ORBITAL PLANE PRECESSION

In cases where the secondary's spin and the orbital angular momentum are not initially aligned, the orbital plane and spin will subsequently precess during the inspiral. To capture this motion we evolve the inspiral using the osculating element equations we derived in Sec. IV, though with the initial condition  $\iota_0 = \pi/4$  to avoid coordinate divergences in the osculating element equations (recall the discussion at the end of Sec. IV B). In the previous section the influence of a spin-aligned secondary on the inspiral phase was assessed by comparing to a non-spinning inspiral with the same two initial orbital frequencies. In the case of generic spin orientation there are three orbital frequencies, the additional one associated with the precession of the orbital plane. It may be possible to make a matched-frequency comparison between a spin-unaligned inspiral in Schwarzschild spacetime and an inspiral with a non-spinning secondary in Kerr spacetime. At the present time fully relativistic, generic orbit Kerr inspirals are not available for comparison (though kludge models do exist for this case [20]). Our waveform generation scheme, presented in Sec. VI A, is only appli-

cable to inspirals in the equatorial plane. Consequently, in this section we showcase generic spin inspirals without assessing the effect of the spin on the inspiral phase or attempting to compute the associated waveforms (these are left for future work).

#### A. Consistency checks

To test whether our numerical code is functioning correctly we performed a number of consistency checks. As discussed in Sec. V B, if the self-force is not applied the spinning secondary's worldline admits a constant of motion for each of the spacetime's Killing vectors [111]. The time-like killing vector of Schwarzschild spacetime results in a conserved specific energy  $\mathcal{E}^S$ . The presence of spin perturbs the geodesic specific energy  $\mathcal{E}^G$  by  $\Delta\mathcal{E}$

$$\mathcal{E}^S = \mathcal{E}^G + \Delta\mathcal{E}, \quad (8.1)$$

$$\Delta\mathcal{E} = \frac{M}{\mu} \sin\theta_p (u^\theta S^\varphi - u^\varphi S^\theta). \quad (8.2)$$

Additionally, the three rotational killing vectors imply conservation of the  $x$ ,  $y$ , and  $z$  components of angular momentum. The  $z$ -component is given by

$$\mathcal{L}_z^S = \mathcal{L}_z^G + \Delta\mathcal{L}_z, \quad (8.3)$$

$$\mathcal{L}_z^G = r_p^2 u^\varphi \sin^2\theta_p, \quad (8.4)$$

$$\Delta\mathcal{L}_z = \frac{1}{\mu} \left( f_p r_p (S^t u^\theta - S^\theta u^t) \sin\theta_p + (S^r u^t - S^t u^r) \cos\theta_p \right). \quad (8.5)$$

Similar results are straightforwardly obtained for the  $x$  and  $y$  components of the angular momentum. Fig. 5 demonstrates that the perturbed energy  $\mathcal{E}^S$  and  $z$ -component of angular momentum  $\mathcal{L}_z^S$  are conserved along the worldline if application of the self-force is withheld. As a further consistency check we verified that the spin magnitude is invariant under parallel transport.

#### B. Sample results

The larger the mass ratio, the more prominent the precession of the orbital plane will be. In order to make the precession due to the spin-curvature force visible we computed an inspiral with mass-ratio  $\epsilon = 0.08$  and spin magnitude  $s = 1$ . Computing an inspiral at this mass ratio is a slight abuse of perturbation theory, as we are not sure of its validity for these values of  $\epsilon$  (though see e.g., [37] which suggests the range of validity of black hole perturbation theory might be larger than once thought). Our results for this  $\epsilon = 0.08$  inspiral are presented in Fig. 6. In displaying our results we rotate the coordinates such that the new inclination parameter oscillates around zero (recall that  $\iota_0 = \pi/4$ ), or equivalently, the new  $z$ -coordinate of the position vector,  $z_p''$ , oscillates with a

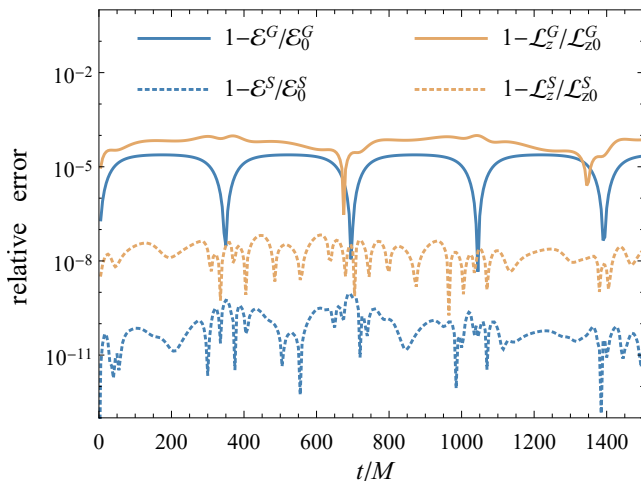


FIG. 5. Energy ( $\mathcal{E}^S$ ) and angular momentum ( $z$ -component  $\mathcal{L}_z^S$ ) conservation in the presence of spin-curvature force alone. Numerical residuals (relative errors) from expected strict conservation in energy and angular momentum are shown (dotted curves) for an orbit in which spin-curvature force is applied but the self-force is not. For contrast, the strictly geodesic quantities  $\mathcal{E}^G$  and  $\mathcal{L}_z^G$  (solid curves) can be seen to vary with an amplitude on the order of the mass ratio  $\epsilon$ . The orbital parameters in this example are  $e_0 = 0.3$ ,  $p_0 = 10$ ,  $\iota_0 = \pi/4$ ,  $S_0^r = S_0^\theta M = S_0^\varphi M = 0.3\mu^2$ ,  $\epsilon = 10^{-3}$ .

minimized amplitude. The transformation to the double primed coordinate system is given by

$$\begin{bmatrix} x_p \\ y_p \\ z_p \end{bmatrix} = \begin{bmatrix} 1 & 0 & 0 \\ 0 & \cos \iota_0 & -\sin \iota_0 \\ 0 & \sin \iota_0 & \cos \iota_0 \end{bmatrix} \begin{bmatrix} x_p'' \\ y_p'' \\ z_p'' \end{bmatrix}. \quad (8.6)$$

For the orbital parameters chosen in Fig. 6,  $z_p''$  reaches 4% of  $r_p$  at its maximum. At this level, precession of the orbital plane is noticeable but modest.

## IX. CONCLUSIONS

In this work we have computed the effect of spin-curvature coupling on the inspiral of a spinning body into a non-rotating black hole including all first-order in the mass-ratio self-force effects. For binaries where the spin and orbital angular momentum are aligned or anti-aligned we compute the waveforms by evolving through a sequence of snapshot waveforms. We also computed the dephasing of these waveforms with respect to non-spinning binaries, finding that the sign of the accumulated phase difference depends on the initial binary separation. For binaries with initial eccentricity  $e_0 = 0$  the phase accumulation for a spin-aligned binary versus a non-spinning binary is negative for  $p \gtrsim 30$  and positive for  $p \lesssim 30$  (spin anti-aligned binaries show the opposite behavior). For binaries with initial eccentricity  $e_0 = 0.75$  the change in sign of the accumulated phase difference

occurs for  $p \simeq 20$ . The magnitude of the dephasing due to the spin-curvature force is similar in magnitude to the conservative self-force corrections to the inspiral phase [58]. We leave it to future work to examine whether inspirals computed using, e.g., a radiative approximation with a spinning secondary can mimic inspirals computed using the full dissipative and conservative self-force for a non-spinning binary. For orbits where the spin and orbital angular-momentum are not aligned the secondary will precess out of the equatorial plane. We extend the osculating element prescription of motion to accommodate this precession and present an example inspiral in Fig. 6.

This work is naturally extended in a number of ways. First, our primary is not rotating. For a rotating primary there are self-force calculations (in the radiation gauge) [121], efficient calculations of the spin-curvature force [111], and osculating element schemes [77]. These three pieces could be combined to extend the results in this work. Second, we do not include second-order in the mass-ratio fluxes or fluxes related the spinning secondary in this work. Work progresses calculating the former [47–56]. The latter has been calculated for circular orbits [78–80] but has not, to the best of our knowledge, been calculated for generic orbits. As per the discussion in Sec. II, inclusion of these pieces is necessary to get a waveform accurate to post-1-adiabatic order. Third, because of the geodesic self-force approximation we use in this work, it is important to compare our inspirals against those from computed using self-consistent evolutions [59, 73–75].

Finally we note that, although our evolution scheme is primarily based upon numerical self-force results, there is much scope for synergy with analytic results. Recently, combining black hole perturbation and post-Newtonian theory has allowed for the calculation of gauge invariant results to very high post-Newtonian order (at first-order in the mass-ratio) [28, 30, 35, 39–41, 122–124]. These results are often to such high order that they reproduce strong-field results to better than a fraction of a percent. As we argued in our previous paper [58] (and is also noted in [60]), whilst the leading-order flux needs to be calculated to better than one part in the inverse mass-ratio, the terms that contribute to the post-1-adiabatic evolution need only be calculated to one part in a thousand. Even in the strong-field, the accuracy requirement for the latter is within the reach of high-order post-Newtonian black hole perturbation theory results. We thus envisage these high-order post-Newtonian results complementing high accuracy numerical calculations like those presented in this work.

## ACKNOWLEDGMENTS

We thank Zach Nasipak for computational assistance. This work was supported in part by NSF grant PHY-1506182. N.W. gratefully acknowledges support from a Marie Curie International Outgoing Fellowship (PIOF-

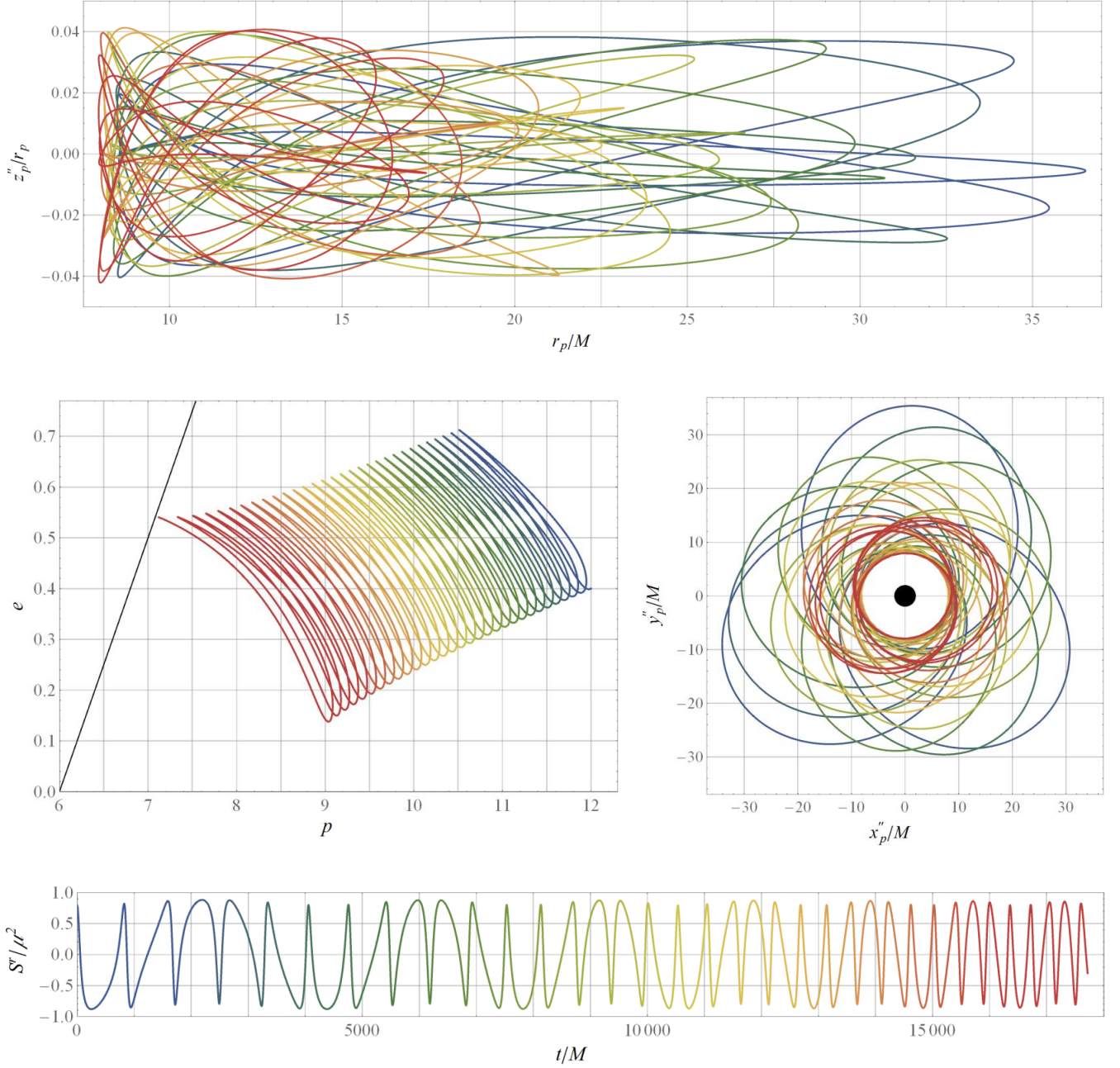


FIG. 6. Sample inspiral with mass ratio  $\epsilon = 0.08$  and  $|s| = 1$  and initial parameters  $p_0 = 12$ ,  $e_0 = 0.4$ ,  $\iota_0 = \pi/4$ ,  $S_0^r = 0.7955930287154575\mu^2$ ,  $S_0^\theta M = S_0^\varphi M = 0.03977965143577288\mu^2$ . Changes in color represent the passage of time (blue is  $t = 0$  and red is immediately before plunge). Top:  $z''_p/r_p$  is plotted vs.  $r_p$  to demonstrate precession of the orbital plane. With this large mass-ratio the  $z$ -coordinate of the position vector reaches 4% of  $r_p$  at its maximum. Middle-left: Evolution of the binary through  $(p, e)$  space. The large oscillations in the best-fit (osculating) geodesics are a result of the high mass ratio. The black line is the separatrix. Middle-right: A top-down view of the trajectory in Schwarzschild coordinates. From this viewpoint the trajectory resembles that of an equatorial inspiral because the precession is modest. Bottom: The  $r$ -component of the spin-vector is plotted vs.  $t$ . On short timescales  $S^r$  exhibits bi-periodicity where the fundamental frequencies are the radial frequency and the frequency of spin precession.

GA-2012-627781). C.R.E. acknowledges support from

the Bahnson Fund at the University of North Carolina-Chapel Hill.

### Appendix A: Osculating element equations

The coefficients that appear in Eq. (4.33) are given by

$$c_e^{(t)} = \frac{(2e^2 - p + 6) [(3e^2 - 4p + 12) \cos v + e(e \cos(3v) + (6 - p) \cos(2v))] + e(p(3p - 32) + 60 - 2e^2(p - 10))}{2\mu M^{-1} p^{-1} (p - 3 - e^2)^{-1} [(p - 2)^2 - 4e^2]^{-1/2} [(p - 6)^2 - 4e^2] (1 + e \cos v)^4 \sqrt{p - 6 - 2e \cos v}}, \quad (\text{A1})$$

$$c_e^{(r)} = \frac{Mp^2(1 - e^2)(p - 3 - e^2) ((p - 6)(p - 2) + 4e^2) \sin v}{\mu ((p - 6)^2 - 4e^2) (p - 2 - 2e \cos v)(1 + e \cos v)^4}, \quad (\text{A2})$$

$$c_p^{(t)} = \frac{Mp^2(p - 3 - e^2) [e^2 \cos(2v) + e^2 - 2p + 6] \sqrt{(p - 6 - 2e \cos v)[(p - 2)^2 - 4e^2]}}{\mu [(p - 6)^2 - 4e^2] (1 + e \cos v)^4}, \quad (\text{A3})$$

$$c_p^{(r)} = \frac{2eM(p - 4)^2 p^3 (e^2 - p + 3) \sin v}{\mu (2e \cos v - p + 2)(1 + e \cos v)^4 [4e^2 - (p - 6)^2]}, \quad (\text{A4})$$

$$c_{\chi_0}^{(t)} = \frac{Mp \sin v (e^2 - p + 3) [e(4e^2 - (p - 6)^2) \cos v + (p - 6)(e^2 \cos(2v) + e^2 - 2p + 6)] \sqrt{(p - 2)^2 - 4e^2}}{\mu e ((p - 6)^2 - 4e^2) (1 + e \cos v)^4 \sqrt{p - 6 - 2e \cos v}}, \quad (\text{A5})$$

$$c_{\chi_0}^{(r)} = \frac{Mp^2(p - 3 - e^2) [(4e^4 - e^2((p - 8)p + 24) - (p - 6)(p - 2)) \cos v - 2e(p - 4)^2]}{\mu e (4e^2 - (p - 6)^2) (1 + e \cos v)^4 (2e \cos v - p + 2)}. \quad (\text{A6})$$

The coefficients that appear in Eq. (4.35) are given by

$$c_\iota^{(\theta)} = \frac{M^2 p^{5/2} \cos \varphi'_p (e^2 - p + 3)}{\mu \cos \iota (1 + e \cos v)^4} \sqrt{\frac{1 - \sin^2 \iota \sin^2 \varphi'_p}{p - 6 - 2e \cos v}}, \quad (\text{A7})$$

$$c_\iota^{(e)} = \frac{\sin \iota \cos^2 \varphi'_p (e - (e^2 - 2p + 6) \cos v)}{\cos \iota (e^2 - p + 3) (1 + e \cos v)}, \quad (\text{A8})$$

$$c_\iota^{(p)} = \frac{(6 + 2e^2 - 3p) \cos^2 \varphi'_p \sin \iota}{2p \cos \iota (3 + e^2 - p)}, \quad (\text{A9})$$

$$c_\iota^{(\chi_0)} = -\frac{2e \sin \iota \sin v \cos^2 \varphi'_p}{\cos \iota (1 + e \cos v)}, \quad (\text{A10})$$

$$c_\Phi^{(\theta)} = \frac{M^2 p^{5/2} \sin \varphi'_p (p - 3 - e^2)}{\mu \sin \iota (1 + e \cos v)^4} \sqrt{\frac{1 - \sin^2 \iota \sin^2 \varphi'_p}{p - 6 - 2e \cos v}}, \quad (\text{A11})$$

$$c_\Phi^{(e)} = \frac{\sin(2\varphi'_p) ((e^2 - 2p + 6) \cos v - e)}{2(e^2 - p + 3)(1 + e \cos v)} + \frac{(2e + p - 6)\bar{F} - (p - 6)\bar{E}}{e(2e + p - 6)} \sqrt{\frac{p}{p - 6 - 2e}} - \frac{2(p - 6) \sin v}{((p - 6)^2 - 4e^2)} \sqrt{\frac{p}{(p - 6 - 2e \cos v)}}, \quad (\text{A12})$$

$$c_\Phi^{(p)} = -\frac{4p^{1/2} (p - 3 - e^2) \sqrt{p - 6 - 2e} ((2e + p - 6)\bar{F} - p\bar{E}) + (2e^2 - 3p + 6)(2e - p + 6)(2e + p - 6) \sin(2\varphi'_p)}{4p(p - 6 - 2e)(p - 6 + 2e)(p - 3 - e^2)} + \frac{2e \sin v}{(p - 6)^2 - 4e^2} \sqrt{\frac{p}{p - 6 - 2e \cos v}}, \quad (\text{A13})$$

$$c_\Phi^{(\chi_0)} = \frac{e \sin v \sin(2\varphi'_p)}{1 + e \cos v} - \sqrt{\frac{p}{p - 6 - 2e \cos v}}, \quad (\text{A14})$$

where  $\bar{F}$  and  $\bar{E}$  are the incomplete elliptic integrals of the first and second kind, respectively, each with the same

arguments as the elliptic integral in Eq. (4.13). The coefficients that appear in Eq. (4.36) are given by

$$c_{\Omega}^{(e)} = \frac{4p^{1/2} \cos \iota (\sqrt{p-6-2e}((p-6)\bar{E} - (2e+p-6)\bar{F})\sqrt{p-6-2e \cos v} + 2e(p-6) \sin v)}{e(2e-p+6)(2e+p-6)\sqrt{p-6-2e \cos v} (2 \sin^2 \iota \cos(2\varphi') + \cos(2\iota) + 3)}, \quad (\text{A15})$$

$$c_{\Omega}^{(p)} = \frac{4 \cos \iota ((2e-p+6)((2e+p-6)\bar{F} - p\bar{E})\sqrt{p-6-2e \cos v} + 2ep\sqrt{p-6-2e} \sin v)}{(p-6-2e)^{3/2}(2e+p-6)\sqrt{p(p-6-2e \cos v)} (2 \sin^2 \iota \cos(2\varphi) + \cos(2\iota) + 3)}, \quad (\text{A16})$$

$$c_{\Omega}^{(\chi_0)} = \frac{4 \cos \iota}{2 \sin^2 \iota \cos(2\varphi'_p) + \cos(2\iota) + 3} \sqrt{\frac{p}{p-6-2e \cos v}}, \quad (\text{A17})$$

$$c_{\Omega}^{(\iota)} = \frac{2 \sin \iota \sin(2\varphi'_p)}{2 \sin^2 \iota \cos(2\varphi'_p) + \cos(2\iota) + 3}, \quad (\text{A18})$$

$$c_{\Omega}^{(\Phi)} = -\frac{4 \cos \iota}{2 \sin^2 \iota \cos(2\varphi'_p) + \cos(2\iota) + 3}. \quad (\text{A19})$$

- 
- [1] B. P. Abbott *et al.* (LIGO Scientific Collaboration and Virgo Collaboration), *Phys. Rev. Lett.* **116**, 061102 (2016).
- [2] B. P. Abbott *et al.* (LIGO Scientific Collaboration and Virgo Collaboration), *Phys. Rev. Lett.* **116**, 241103 (2016), [arXiv:1606.04855](#).
- [3] B. P. Abbott *et al.* (LIGO Scientific Collaboration and Virgo Collaboration), *Phys. Rev. Lett.* **118**, 221101 (2017), [arXiv:1706.01812](#).
- [4] P. Amaro-Seoane *et al.*, ArXiv e-prints (2017), [arXiv:1702.00786](#).
- [5] S. Babak, J. Gair, A. Sesana, E. Barausse, C. F. Sopuerta, C. P. L. Berry, E. Berti, P. Amaro-Seoane, A. Petiteau, and A. Klein, (2017), [arXiv:1703.09722](#).
- [6] S. J. Vigeland and S. A. Hughes, *Phys. Rev. D* **81**, 024030 (2010), [arXiv:0911.1756](#).
- [7] L. Barack and C. Cutler, *Phys. Rev. D* **75**, 042003 (2007), [arXiv:gr-qc/0612029](#).
- [8] D. A. Brown, J. Brink, H. Fang, J. R. Gair, C. Li, G. Lovelace, I. Mandel, and K. S. Thorne, *Physical Review Letters* **99**, 201102 (2007), [gr-qc/0612060](#).
- [9] J. R. Gair, M. Vallisneri, S. L. Larson, and J. G. Baker, *Living Rev. Rel.* **16**, 7 (2013), [arXiv:1212.5575](#).
- [10] E. Barausse, V. Cardoso, and P. Pani, *Phys. Rev. D* **89**, 104059 (2014), [arXiv:1404.7149](#).
- [11] D. A. Brown, H. Fang, J. R. Gair, C. Li, G. Lovelace, I. Mandel, and K. S. Thorne, *Phys. Rev. Lett.* **99**, 201102 (2007), [arXiv:gr-qc/0612060](#).
- [12] E. A. Huerta and J. R. Gair, *Phys. Rev. D* **83**, 044020 (2011), [arXiv:1009.1985](#).
- [13] E. A. Huerta and J. R. Gair, *Phys. Rev. D* **83**, 044021 (2011), [arXiv:1011.0421](#).
- [14] M. C. Miller, *Astrophys. J.* **581**, 438 (2002), [arXiv:astro-ph/0206404](#).
- [15] A. Sesana, *Phys. Rev. Lett.* **116**, 231102 (2016), [arXiv:1602.06951](#).
- [16] M. C. Miller, *Astrophys. J.* **618**, 426 (2004), [arXiv:astro-ph/0409331](#) [astro-ph].
- [17] I. Mandel, D. A. Brown, J. R. Gair, and M. C. Miller, *Astrophys. J.* **681**, 1431 (2008), [arXiv:0705.0285](#).
- [18] S. Drasco and S. A. Hughes, *Phys. Rev. D* **69**, 044015 (2004).
- [19] R. Fujita, W. Hikida, and H. Tagoshi, *Prog. Theor. Phys.* **121**, 843 (2009), [arXiv:0904.3810](#).
- [20] S. Babak, H. Fang, J. R. Gair, K. Glampedakis, and S. A. Hughes, *Phys. Rev. D* **75**, 024005 (2007), [Erratum: *Phys. Rev. D* **77**, 04990(2008)], [arXiv:gr-qc/0607007](#).
- [21] T. Hinderer and E. E. Flanagan, *Phys. Rev. D* **78**, 064028 (2008), [arXiv:0805.3337](#).
- [22] E. Poisson, A. Pound, and I. Vega, *Living Rev. Rel.* **14**, 7 (2011), [arXiv:gr-qc/1102.0529](#).
- [23] S. Detweiler, *Phys. Rev. D* **77**, 124026 (2008), [arXiv:0804.3529](#).
- [24] L. Barack and N. Sago, *Phys. Rev. Lett.* **102**, 191101 (2009), [arXiv:0902.0573](#).
- [25] L. Barack and N. Sago, *Phys. Rev. D* **83**, 084023 (2011), [arXiv:1101.3331](#).
- [26] S. R. Dolan, N. Warburton, A. I. Harte, A. Le Tiec, B. Wardell, and L. Barack, *Phys. Rev. D* **89**, 064011 (2014), [arXiv:1312.0775](#).
- [27] S. R. Dolan, P. Nolan, A. C. Ottewill, N. Warburton, and B. Wardell, *Phys. Rev. D* **91**, 023009 (2015), [arXiv:1406.4890](#).
- [28] P. Nolan, C. Kavanagh, S. R. Dolan, A. C. Ottewill, N. Warburton, and B. Wardell, *Phys. Rev. D* **92**, 123008 (2015), [arXiv:1505.04447](#).
- [29] S. Akcay, A. Le Tiec, L. Barack, N. Sago, and N. Warburton, *Phys. Rev. D* **91**, 124014 (2015), [arXiv:1503.01374](#).
- [30] A. G. Shah and A. Pound, *Phys. Rev. D* **91**, 124022 (2015), [arXiv:1503.02414](#).
- [31] A. G. Shah, J. L. Friedman, and B. F. Whiting, *Phys. Rev. D* **89**, 064042 (2014), [arXiv:1312.1952](#).
- [32] S. Isoyama, L. Barack, S. R. Dolan, A. Le Tiec, H. Nakano, A. G. Shah, T. Tanaka, and N. Warburton, *Phys. Rev. Lett.* **113**, 161101 (2014), [arXiv:1404.6133](#).
- [33] M. van de Meent and A. G. Shah, *Phys. Rev. D* **92**, 064025 (2015), [arXiv:1506.04755](#).
- [34] M. van de Meent, *Phys. Rev. Lett.* **118**, 011101 (2017), [arXiv:1610.03497](#).
- [35] C. Kavanagh, A. C. Ottewill, and B. Wardell, *Phys.*

- Rev. D* **92**, 084025 (2015), arXiv:1503.02334.
- [36] L. Blanchet, S. Detweiler, A. Le Tiec, and B. F. Whiting, *Phys. Rev. D* **81**, 064004 (2010), arXiv:0910.0207.
- [37] A. Le Tiec, A. H. Mroué, L. Barack, A. Buonanno, H. P. Pfeiffer, N. Sago, and A. Taracchini, *Phys. Rev. Lett.* **107**, 141101 (2011), arXiv:1106.3278.
- [38] S. Akcay, L. Barack, T. Damour, and N. Sago, *Phys. Rev. D* **86**, 104041 (2012), arXiv:1209.0964.
- [39] D. Bini and T. Damour, *Phys. Rev. D* **89**, 064063 (2014), arXiv:1312.2503.
- [40] D. Bini and T. Damour, *Phys. Rev. D* **90**, 024039 (2014), arXiv:1404.2747.
- [41] D. Bini and T. Damour, *Phys. Rev. D* **90**, 124037 (2014), arXiv:1409.6933.
- [42] A. Zimmerman, A. G. M. Lewis, and H. P. Pfeiffer, *Phys. Rev. Lett.* **117**, 191101 (2016), arXiv:1606.08056.
- [43] S. Akcay, D. Dempsey, and S. Dolan, *Class. Quant. Grav.* **34**, 084001 (2017), arXiv:1608.04811.
- [44] E. E. Flanagan and T. Hinderer, *Phys. Rev. Lett.* **109**, 071102 (2012), arXiv:1009.4923.
- [45] J. Brink, M. Geyer, and T. Hinderer, *Phys. Rev. Lett.* **114**, 081102 (2015), arXiv:1304.0330.
- [46] U. Ruangsri and S. A. Hughes, *Phys. Rev. D* **89**, 084036 (2014), arXiv:1307.6483.
- [47] A. Pound, *Phys. Rev. Lett.* **109**, 051101 (2012), arXiv:1201.5089.
- [48] S. E. Gralla, *Phys. Rev. D* **85**, 124011 (2012), arXiv:1203.3189.
- [49] S. Detweiler, *Phys. Rev. D* **85**, 044048 (2012), arXiv:1107.2098.
- [50] A. Pound, *Phys. Rev. D* **90**, 084039 (2014), arXiv:1404.1543.
- [51] N. Warburton and B. Wardell, *Phys. Rev. D* **89**, 044046 (2014), arXiv:1311.3104.
- [52] A. Pound and J. Miller, *Phys. Rev. D* **89**, 104020 (2014), arXiv:1403.1843.
- [53] B. Wardell and N. Warburton, *Phys. Rev. D* **92**, 084019 (2015), arXiv:1505.07841.
- [54] A. Pound, *Phys. Rev. D* **92**, 104047 (2015), arXiv:1510.05172.
- [55] J. Miller, B. Wardell, and A. Pound, *Phys. Rev. D* **94**, 104018 (2016), arXiv:1608.06783.
- [56] A. Pound, *Phys. Rev. D* **95**, 104056 (2017), arXiv:1703.02836.
- [57] N. Warburton, S. Akcay, L. Barack, J. R. Gair, and N. Sago, *Phys. Rev. D* **85**, 061501 (2012), arXiv:1111.6908.
- [58] T. Osburn, N. Warburton, and C. R. Evans, *Phys. Rev. D* **93**, 064024 (2016), arXiv:1511.01498.
- [59] P. Diener, I. Vega, B. Wardell, and S. Detweiler, *Physical Review Letters* **108**, 191102 (2012), arXiv:1112.4821.
- [60] E. A. Huerta and J. R. Gair, *Phys. Rev. D* **84**, 064023 (2011), arXiv:1105.3567.
- [61] E. A. Huerta, J. R. Gair, and D. A. Brown, *Phys. Rev. D* **85**, 064023 (2012), arXiv:1111.3243.
- [62] L. M. Burko and G. Khanna, *Phys. Rev. D* **91**, 104017 (2015), arXiv:1503.05097.
- [63] A. Papapetrou, *Proc. R. Soc. Lond.* **A209**, 248 (1951).
- [64] W. G. Dixon, *Royal Society of London Proceedings Series A* **314**, 499 (1970).
- [65] S. A. Hughes, S. Drasco, E. E. Flanagan, and J. Franklin, *Phys. Rev. Lett.* **94**, 221101 (2005), arXiv:gr-qc/0504015.
- [66] S. Drasco, E. E. Flanagan, and S. A. Hughes, *Classical and Quantum Gravity* **22**, S801 (2005).
- [67] T. Tanaka, *Progress of Theoretical Physics Supplement* **163**, 120 (2006), gr-qc/0508114.
- [68] S. Drasco and S. A. Hughes, *Phys. Rev. D* **73**, 024027 (2006), gr-qc/0509101.
- [69] M. D. Hartl, *Phys. Rev. D* **67**, 024005 (2003), arXiv:gr-qc/0210042.
- [70] S. Akcay, N. Warburton, and L. Barack, *Phys. Rev. D* **88**, 104009 (2013), arXiv:1308.5223.
- [71] T. Osburn, E. Forseth, C. R. Evans, and S. Hopper, *Phys. Rev. D* **90**, 104031 (2014), arXiv:1409.4419.
- [72] A. Pound, *Proceedings, 524th WE-Heraeus-Seminar: Equations of Motion in Relativistic Gravity (EOM 2013)*, *Fund. Theor. Phys.* **179**, 399 (2015), arXiv:1506.06245.
- [73] N. Warburton (2013), Talk presented at the 16th Capra meeting held at University College Dublin, <http://maths.ucd.ie/capra16/schedule/>.
- [74] N. Warburton (2014), Talk presented at the 17th Capra meeting held at Caltech, <http://www.tapir.caltech.edu/~capra17/Schedule.shtml>.
- [75] P. Diener (2015), Talk presented at the 18th Capra meeting held at Kyoto University, <http://www2.yukawa.kyoto-u.ac.jp/~capra18/>.
- [76] A. Pound and E. Poisson, *Phys. Rev. D* **77**, 044013 (2008), arXiv:0708.3033.
- [77] J. R. Gair, É. É. Flanagan, S. Drasco, T. Hinderer, and S. Babak, *Phys. Rev. D* **83**, 044037 (2011), arXiv:1012.5111.
- [78] E. Harms, G. Lukes-Gerakopoulos, S. Bernuzzi, and A. Nagar, *Phys. Rev. D* **94**, 104010 (2016), arXiv:1609.00356.
- [79] E. Harms, G. Lukes-Gerakopoulos, S. Bernuzzi, and A. Nagar, *Phys. Rev. D* **93**, 044015 (2016), arXiv:1510.05548.
- [80] W.-B. Han, *Phys. Rev. D* **82**, 084013 (2010), arXiv:1008.3324 [gr-qc].
- [81] C. Cutler, D. Kennefick, and E. Poisson, *Phys. Rev. D* **50**, 3816 (1994).
- [82] C. Darwin, *Proc. R. Soc. Lond. A* **249**, 180 (1959).
- [83] R. Fujita and W. Hikida, *Classical and Quantum Gravity* **26**, 135002 (2009), arXiv:0906.1420.
- [84] S. L. Detweiler and E. Poisson, *Phys. Rev. D* **69**, 084019 (2004), arXiv:gr-qc/0312010.
- [85] L. Barack and C. O. Lousto, *Phys. Rev. D* **72**, 104026 (2005), arXiv:gr-qc/0510019.
- [86] M. Berndston, *Harmonic Gauge Perturbations of the Schwarzschild Metric*, Ph.D. thesis, University of Colorado (2007), arXiv:0904.0033v1.
- [87] L. Barack and N. Sago, *Phys. Rev. D* **81**, 084021 (2010), arXiv:1002.2386.
- [88] S. Hopper and C. R. Evans, *Phys. Rev. D* **82**, 084010 (2010), arXiv:1006.4907.
- [89] S. Akcay, *Phys. Rev. D* **83**, 124026 (2011).
- [90] S. Hopper and C. R. Evans, *Phys. Rev. D* **87**, 064008 (2013), arXiv:1210.7969.
- [91] S. Hopper, E. Forseth, T. Osburn, and C. R. Evans, *Phys. Rev. D* **92**, 044048 (2015), arXiv:1506.04742.
- [92] Y. Mino, M. Sasaki, and T. Tanaka, *Phys. Rev. D* **55**, 3457 (1997).
- [93] T. C. Quinn and R. M. Wald, *Phys. Rev. D* **56**, 3381 (1997).

- [94] L. Barack and A. Ori, *Phys. Rev. D* **61**, 061502 (2000), [arXiv:gr-qc/9912010](#).
- [95] L. Barack, *Phys. Rev. D* **64**, 084021 (2001), [arXiv:gr-qc/0105040](#).
- [96] L. Barack, Y. Mino, H. Nakano, A. Ori, and M. Sasaki, *Physical Review Letters* **88**, 091101 (2002), [gr-qc/0111001](#).
- [97] L. Barack and A. Ori, *Phys. Rev. D* **67**, 024029 (2003), [arXiv:gr-qc/0209072](#).
- [98] S. Detweiler, E. Messaritaki, and B. F. Whiting, *Phys. Rev. D* **67**, 104016 (2003), [arXiv:gr-qc/0205079](#).
- [99] A. Heffernan, A. Ottewill, and B. Wardell, *Phys. Rev. D* **86**, 104023 (2012), [arXiv:1204.0794](#).
- [100] A. Heffernan, A. Ottewill, and B. Wardell, *Phys. Rev. D* **89**, 024030 (2014), [arXiv:1211.6446](#).
- [101] A. Pound, C. Merlin, and L. Barack, *Phys. Rev. D* **89**, 024009 (2014), [arXiv:1310.1513](#).
- [102] L. Barack and N. Sago, *Phys. Rev. D* **75**, 064021 (2007), [arXiv:gr-qc/0701069](#).
- [103] S. R. Dolan and L. Barack, *Phys. Rev. D* **87**, 084066 (2013), [arXiv:1211.4586](#).
- [104] T. Regge and J. Wheeler, *Phys. Rev.* **108**, 1063 (1957).
- [105] F. Zerilli, *Phys. Rev. D* **2**, 2141 (1970).
- [106] M. Mathisson, *General Relativity and Gravitation* **42**, 1011 (2010).
- [107] L. F. O. Costa and J. Natrio, *Proceedings, 524th WE-Heraeus-Seminar: Equations of Motion in Relativistic Gravity (EOM 2013): Bad Honnef, Germany, February 17-23, 2013*, *Fund. Theor. Phys.* **179**, 215 (2015), [arXiv:1410.6443](#).
- [108] K. Kyrián and O. Semerák, *Mon. Not. R. Astron. Soc* **382**, 1922 (2007).
- [109] G. Lukes-Gerakopoulos, J. Seyrich, and D. Kunst, *Phys. Rev. D* **90**, 104019 (2014).
- [110] F. A. E. Pirani, *Acta Physica Polonica* **15**, 389 (1956).
- [111] U. Ruangsri, S. J. Vigeland, and S. A. Hughes, *Phys. Rev. D* **94**, 044008 (2016), [arXiv:1512.00376](#).
- [112] A. Zenginoglu and G. Khanna, *Phys. Rev. X* **1**, 021017 (2011), [arXiv:1108.1816](#).
- [113] P. A. Sundararajan, G. Khanna, S. A. Hughes, and S. Drasco, *Phys. Rev. D* **78**, 024022 (2008), [arXiv:0803.0317](#).
- [114] L. Barack and C. Cutler, *Phys. Rev. D* **69**, 082005 (2004), [arXiv:gr-qc/0310125](#).
- [115] A. J. K. Chua and J. R. Gair, *Class. Quant. Grav.* **32**, 232002 (2015), [arXiv:1510.06245](#).
- [116] S. Teukolsky, *Astrophys. J.* **185**, 635 (1973).
- [117] V. Moncrief, *Ann. Phys.* **88**, 323 (1974).
- [118] C. Cunningham, R. Price, and V. Moncrief, *Astrophys. J.* **224**, 643 (1978).
- [119] C. Cunningham, R. Price, and V. Moncrief, *Astrophys. J.* **230**, 870 (1979).
- [120] M. Campanelli, C. O. Lousto, and Y. Zlochower, *Phys. Rev. D* **74**, 041501 (2006), [arXiv:gr-qc/0604012](#).
- [121] M. van de Meent, *Phys. Rev. D* **94**, 044034 (2016), [arXiv:1606.06297](#).
- [122] C. Kavanagh, A. C. Ottewill, and B. Wardell, *Phys. Rev. D* **93**, 124038 (2016), [arXiv:1601.03394](#).
- [123] E. Forseth, C. R. Evans, and S. Hopper, *Phys. Rev. D* **93**, 064058 (2016), [arXiv:1512.03051](#).
- [124] S. Hopper, C. Kavanagh, and A. C. Ottewill, *Phys. Rev. D* **93**, 044010 (2016), [arXiv:1512.01556](#).